

Flow organization and heat transfer in turbulent wall sheared thermal convection

Alexander Blass^{1†}, Xiaojue Zhu^{1,2}, Roberto Verzicco^{3,1,4},
Detlef Lohse^{1,5} and Richard J.A.M. Stevens^{1‡}

¹Physics of Fluids Group, Max Planck Center for Complex Fluid Dynamics, J. M. Burgers Center for Fluid Dynamics and MESA+ Research Institute, Department of Science and Technology, University of Twente, P.O. Box 217, 7500 AE Enschede, The Netherlands

²Center of Mathematical Sciences and Applications, School of Engineering and Applied Sciences, Harvard University, Cambridge, MA 02138, USA

³Dipartimento di Ingegneria Industriale, University of Rome "Tor Vergata". Via del Politecnico 1, Roma 00133, Italy

⁴Gran Sasso Science Institute - Viale F. Crispi, 7 67100 L'Aquila, Italy.

⁵Max Planck Institute for Dynamics and Self-Organization, Am Fassberg 17, 37077 Göttingen, Germany

(Received xx; revised xx; accepted xx)

We perform direct numerical simulations of wall sheared Rayleigh-Bénard (RB) convection for Rayleigh numbers up to $Ra = 10^8$, Prandtl number unity, and wall shear Reynolds numbers up to $Re_w = 10000$. Using the Monin-Obukhov length L_{MO} we identify three different flow states, a buoyancy dominated regime ($L_{MO} \lesssim \lambda_\theta$; with λ_θ the thermal boundary layer thickness), a transitional regime ($0.5H \gtrsim L_{MO} \gtrsim \lambda_\theta$; with H the height of the domain), and a shear dominated regime ($L_{MO} \gtrsim 0.5H$). In the buoyancy dominated regime the flow dynamics are similar to that of turbulent thermal convection. The transitional regime is characterized by rolls that are increasingly elongated with increasing shear. The flow in the shear dominated regime consists of very large-scale meandering rolls, similar to the ones found in conventional Couette flow. As a consequence of these different flow regimes, for fixed Ra and with increasing shear, the heat transfer first decreases, due to the breakup of the thermal rolls, and then increases at the beginning of the shear dominated regime. For $L_{MO} \gtrsim 0.5H$ the Nusselt number Nu effectively scales as $Nu \sim Ra^\alpha$, with $\alpha \ll 1/3$ while we find $\alpha \simeq 0.31$ in the buoyancy dominated regime. In the transitional regime the effective scaling exponent is $\alpha > 1/3$, but the temperature and velocity profiles in this regime are not logarithmic yet, thus indicating transient dynamics and not the ultimate regime of thermal convection.

1. Introduction

Rayleigh-Bénard (RB) convection, i.e. the flow in a box heated from below and cooled from above, is one of the paradigmatic fluid dynamical systems (Ahlers *et al.* 2009; Lohse & Xia 2010; Chilla & Schumacher 2012; Xia 2013). The dynamics of RB convection are controlled by the Rayleigh number

$$Ra = \beta g H^3 \Delta / (\kappa \nu), \quad (1.1)$$

† Email address for correspondence: a.blass@utwente.nl

‡ Email address for correspondence: r.j.a.m.stevens@utwente.nl

which is the non-dimensional temperature difference between the horizontal plates, and the Prandtl number

$$Pr = \nu/\kappa, \quad (1.2)$$

which is the ratio of momentum and thermal diffusivities. In equations (1.1) and (1.2), H is the non-dimensional distance between the plates, β the thermal expansion coefficient of the fluid, g the gravitational acceleration, Δ the temperature difference between top and bottom plate, and κ and ν the thermal and kinetic diffusivities, respectively. The crucial additional control parameter, whose effect we will analyse in this paper, is the wall shear Reynolds number

$$Re_w = Hu_w/\nu, \quad (1.3)$$

with u_w the velocity of the wall. The ratio between buoyancy and shear driving can be expressed as bulk Richardson number

$$Ri = Ra/(Re_w^2 Pr), \quad (1.4)$$

which can be seen as alternative control parameter for either Ra or Re_w .

Important responses of the system are the Nusselt number

$$Nu = QH/(\kappa\Delta), \quad (1.5)$$

which is the dimensionless vertical heat flux, the friction Reynolds number

$$Re_\tau = Hu_\tau/\nu, \quad (1.6)$$

and the skin friction coefficient

$$C_f = 2\tau_w/\rho u_w^2. \quad (1.7)$$

Here $Q = \overline{w'\theta'} - \kappa\partial T/\partial z$ is the constant vertical heat flux, with w' and θ' the fluctuations for wall-normal velocity and temperature, respectively, and $u_\tau = \sqrt{\tau_w/\rho}$ the friction velocity, with τ_w the mean wall shear stress and ρ the density of the fluid.

For strong enough thermal driving, i.e. high enough Ra , the flow in the bulk region becomes fully turbulent. For even stronger thermal driving, beyond some critical Ra number Ra_c , also the boundary layers become turbulent and the system reaches the regime of so-called ultimate convection (Kraichnan 1962; Grossmann & Lohse 2000, 2001, 2011). This ultimate regime sets in when the shear Reynolds number at the boundary layers is sufficiently high so that the boundary layer becomes turbulent, leading to a strong increase in the heat transport, quantified by the Nusselt number.

Ahlers *et al.* (2012) found that the transition to the ultimate regime sets in around $Ra_c \sim \mathcal{O}(10^{14})$. While in the classical regime one generally finds $Nu \sim Ra^{0.31}$, in the ultimate regime $Nu \sim Ra^{0.38}$, in agreement with theoretical predictions (Grossmann & Lohse 2011).

The transition to the ultimate regime has also been observed in direct numerical simulations (DNS) of two-dimensional RB convection (Zhu *et al.* 2018a). In Taylor-Couette flow, which is a very analogous system, experiments and DNS have observed the ultimate regime as well (Grossmann *et al.* 2016). Such scaling has also been observed in experiments with vertical pipes (Gibert *et al.* 2006; Cholemani & Arakeri 2009; Pawar & Arakeri 2016). However, so far the ultimate regime has not yet been achieved in DNS of three-dimensional RB flows (Stevens *et al.* 2010, 2011) as the required computational time to achieve this is still out of reach. In an attempt to trigger the transition to the ultimate regime, here we add a Couette type shearing to the RB system to increase the shear Reynolds number of the boundary layers.

In Couette flow the top and bottom walls move in opposite directions (Thurlow &

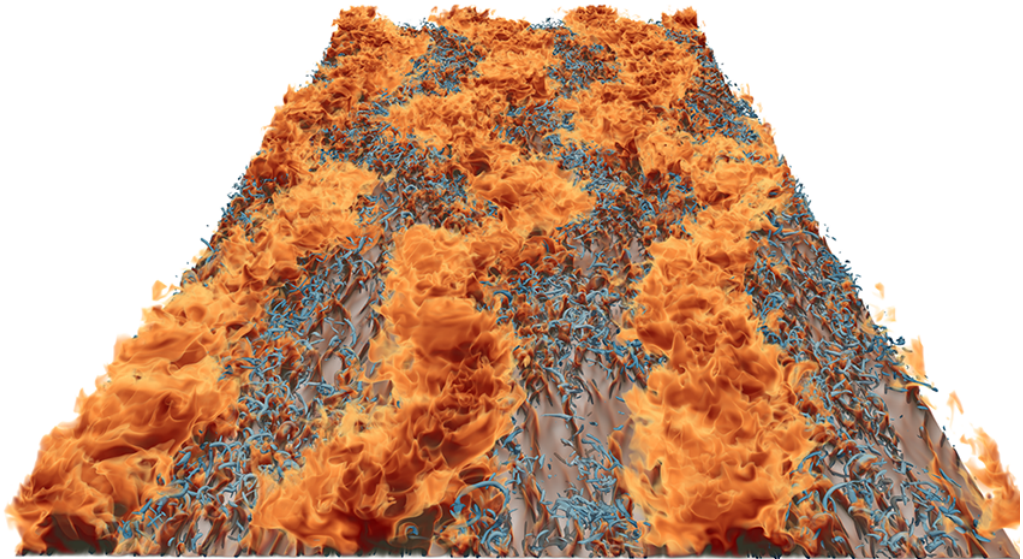


FIGURE 1. Volume rendering of the thermal structures rising from the heated plate in a simulation with $Ra = 2.2 \times 10^6$ and $Re_w = 8000$. The plate dimensions are $9\pi H \times 4\pi H$, in streamwise and spanwise direction, respectively, where H is the distance between the plates. The red colors show hot thermal structures emerging from the hot plate while the blue structures show vorticity formations in the flow. For further details of the flow visualization, please see Favre & Blass (2019).

Klewicki 2000; Barkley & Tuckerman 2005; Tuckerman & Barkley 2011) with constant u_w and just as in other examples of wall bounded turbulence (Jiménez 2018; Smits *et al.* 2011; Smits & Marusic 2013) the flow is dominated by elongated streaks, which have been observed in experiments (Kitoh & Umeki 2008) and DNS (Lee & Kim 1991; Tsukahara *et al.* 2006), even at relatively low shear Reynolds numbers (Chantry *et al.* 2017). Pirozzoli *et al.* (2011, 2014) and Orlandi *et al.* (2015) showed that these streaks in Couette flow have much longer characteristic length scales than in Poiseuille flow, where the flow is forced by a uniform pressure gradient rather than by wall shear. Rawat *et al.* (2015) showed that these large-scale flow structures even survive when the small-scale structures are artificially suppressed. Recently, Lee & Moser (2018) found that the streak length increases with increasing shear Reynolds number and that some correlation in the streamwise direction remains visible up to a length of almost 80 times the distance between the plates.

Investigating the interaction between buoyancy and shear effects is also very important to better understand oceanic and atmospheric flows (Deardorff 1972; Moeng 1984; Khanna & Brasseur 1998). For example early experiments on sheared thermal convection by Ingersoll (1966) and Solomon & Gollub (1990) showed the appearance of large-scale structures. Fukui & Nakajima (1985) showed that in channel flow unstable stratification increases the longitudinal velocity fluctuations close to the wall, while in the bulk region the temperature fluctuations are drastically lowered.

Furthermore, recent experiments by Shevkar *et al.* (2019) investigated the plume spacing in sheared convection and found a scaling law which connects the mean spacing of the plumes with Re_w , Ra , and Pr of the flow.

Early simulations of sheared convection were performed by Hathaway & Somerville (1986) and Domaradzki & Metcalfe (1988) for $Ra \lesssim \mathcal{O}(10^5)$. Domaradzki & Metcalfe

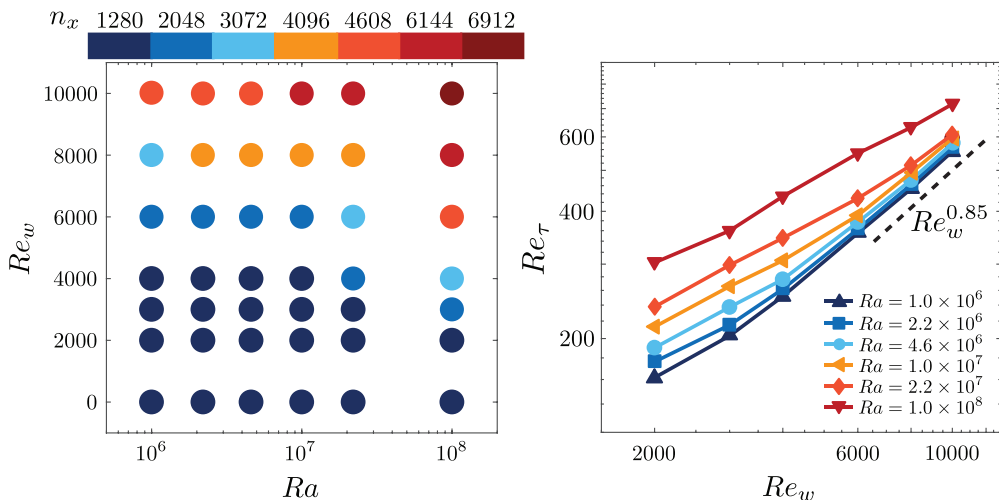


FIGURE 2. (a) Streamwise (n_x) resolution used in the simulations as function of Ra and Re_w , see table 2 for details. (b) Re_τ versus Re_w for the simulations. In agreement with Pirozzoli *et al.* (2014) and Avsarkisov *et al.* (2014), for large Re_w we find $Re_\tau \sim Re_w^{0.85}$.

(1988) found that in Couette-RB flow the addition of shear at low Ra initially increases the heat transport. However, for $Ra \gtrsim 150,000$ the heat transport decreases as the added shear breaks up the large-scale structures. More recently, Scagliarini *et al.* (2014, 2015) showed that also in Poiseuille-RB the heat transfer first decreases when the applied pressure gradient is increased. The reason is that for intermediate forcing the longitudinal wind disturbs the thermal plumes which therefore lose their coherence. Only with a strong enough pressure gradient, a heat transfer enhancement is found. Scagliarini *et al.* (2014) in particular find how Nu depends on Ra , Pr , and Re_τ .

Forced convection in turbulent Couette flow has been investigated theoretically (Choi *et al.* 2004), numerically (Liu 2003; Debusschere & Rutland 2004), and experimentally (Le & Papavassiliou 2006) and shows similar behavior as the high-shear cases of sheared convection.

The Richardson number quantifies the ratio between the buoyancy and shear forces in Couette-RB and Poiseuille-RB based on the applied temperature difference and wall shear Reynolds number. Another way to quantify the ratio between buoyancy and shear forces is to determine the Monin-Obukhov length (Monin & Obukhov 1954; Obukhov 1971)

$$L_{MO}/H = u_\tau^3 / (\overline{w'\theta'} \beta g H), \quad (1.8)$$

which indicates up to which distance from the wall the flow is dominated by shear, based on the observed flow properties. Note that L_{MO}/H is a response parameter, in contrast to Ri , which is a control parameter. Pirozzoli *et al.* (2017) found that the Monin-Obukhov length scales as $L_{MO}/H \approx 0.15/Ri^{0.85}$ for channel flow with unstable stratification.

In this study we investigate the effect of an additional Couette type shearing on the heat transfer in RB convection in an attempt to trigger the boundary layers to become fully turbulent and hence observe the transition to the ultimate regime. Figure 1 shows a flow visualization of the temperature field obtained from one of our simulations, which reveals large-scale meandering streaks that are formed near the hot plate. We performed simulations over a wide parameter range, spanning $10^6 \leq Ra \leq 10^8$ and $0 \leq Re_w \leq 10^4$, while $Pr = 1$ has been used in all cases, see figure 2a. In spite of the very strong forcing for the largest Ra and Re_w , we did not yet achieve ultimate turbulence in this study.

Ra	Pr	Re_w	N_x	N_y	N_z	Re_τ	Ri	L_{MO}/H	Nu	$C_f/10^{-3}$
1.0×10^8	1	10000	1024	512	384	708.0	1.000	0.138	25.66	10.03
1.0×10^8	1	10000	1296	648	384	703.6	1.000	0.137	25.37	9.902
1.0×10^8	1	10000	1536	768	384	700.6	1.000	0.137	25.19	9.818
1.0×10^8	1	10000	1728	864	384	700.0	1.000	0.136	25.15	9.805

TABLE 1. Simulation parameters for the grid study, which is performed in a box of $2\pi H \times \pi H \times H$. The columns from left to right indicate the input and output parameters and the resolution in streamwise, spanwise, and wall-normal direction (N_x, N_y, N_z).

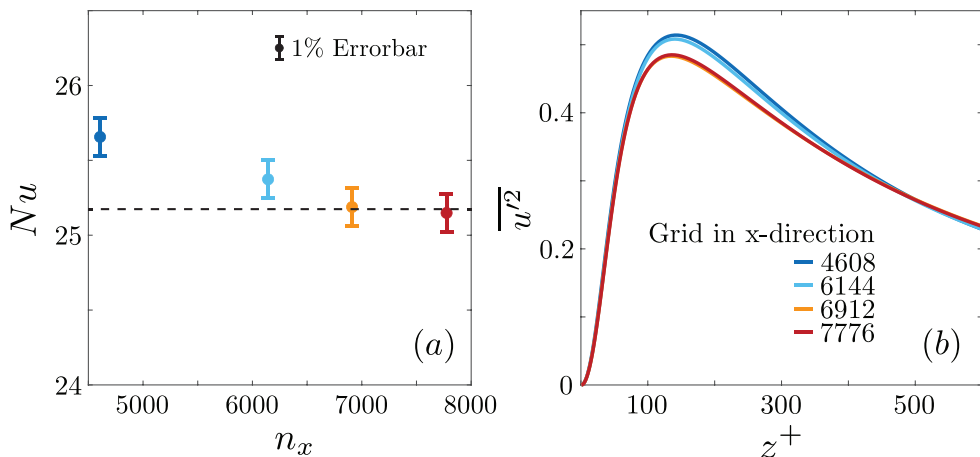


FIGURE 3. (a) Nu and (b) the streamwise velocity fluctuations for simulations at $Ra = 10^8$ and $Re_w = 10000$ performed in a box of $2\pi H \times \pi H \times H$ in streamwise, spanwise, and vertical direction, respectively, on different grids. The displayed resolutions indicate the extrapolated streamwise resolutions that correspond to the full $9\pi H \times 4\pi H \times H$ box, see table 1 for details. Note that the simulation results are converged for the grid resolution used in this study.

We were limited by our own requirement of using large domain sizes as recommended by Pirozzoli *et al.* (2017) to ensure convergence of the main flow properties.

The remainder of this manuscript is organized as follows. In §2 we present the simulation method. We discuss the heat transfer and skin friction measurements in §3.1 and §3.2, respectively. A discussion of the identified flow regimes is given in §4. The concluding remarks follow in §5.

2. Simulation details

We numerically solve the three-dimensional incompressible Navier-Stokes equations within the Boussinesq approximation, which in non-dimensional form read:

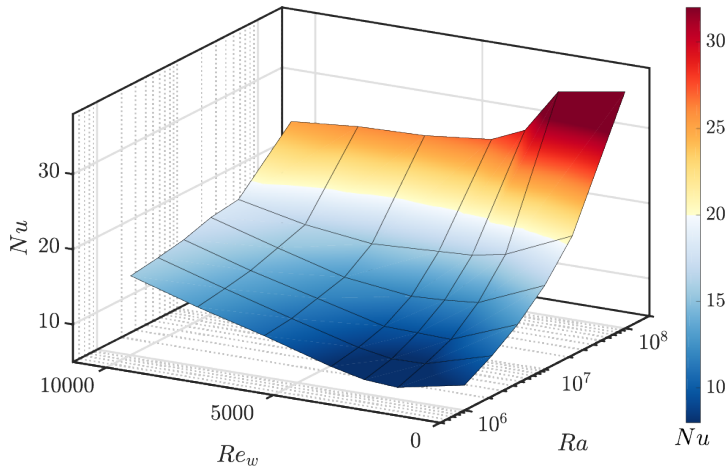
$$\frac{\partial \mathbf{u}}{\partial t} + \mathbf{u} \cdot \nabla \mathbf{u} = -\nabla P + \left(\frac{Pr}{Ra}\right)^{1/2} \nabla^2 \mathbf{u} + \theta \hat{z}, \quad \nabla \cdot \mathbf{u} = 0, \quad (2.1)$$

$$\frac{\partial \theta}{\partial t} + \mathbf{u} \cdot \nabla \theta = \frac{1}{(PrRa)^{1/2}} \nabla^2 \theta, \quad (2.2)$$

with \mathbf{u} the velocity non-dimensionalized by the free-fall velocity $\sqrt{g\beta\Delta H}$, t the dimensionless time normalized by $\sqrt{H/(g\beta\Delta)}$, θ the dimensionless temperature normalized

Ra	Pr	Re_w	N_x	N_y	N_z	Re_τ	Ri	L_{MO}/H	Nu	$C_f/10^{-3}$
0	1	2000	1280	1024	256	134.0	0	0	0	8.971
0	1	3000	1280	1024	256	188.7	0	0	0	7.917
0	1	4000	1280	1024	256	241.8	0	0	0	7.314
0	1	6000	1280	1024	256	346.0	0	0	0	6.651
0	1	8000	2048	1280	256	400.8	0	0	0	5.020
0	1	10000	3072	1536	256	468.0	0	0	0	4.382
1.0×10^6	1	0	1280	1024	256	0	∞	0	8.343	∞
1.0×10^6	1	2000	1280	1024	256	164.2	0.250	0.552	6.557	13.49
1.0×10^6	1	3000	1280	1024	256	206.2	0.111	1.180	6.869	9.449
1.0×10^6	1	4000	1280	1024	256	255.7	0.063	1.983	7.891	8.173
1.0×10^6	1	6000	2048	1280	256	360.7	0.028	4.258	10.52	7.231
1.0×10^6	1	8000	3072	1536	256	459.3	0.016	7.211	12.82	6.592
1.0×10^6	1	10000	4608	2304	320	563.0	0.010	11.00	15.49	6.340
2.2×10^6	1	0	1280	1024	256	0	∞	0	10.40	∞
2.2×10^6	1	2000	1280	1024	256	179.0	0.550	0.306	7.866	16.03
2.2×10^6	1	3000	1280	1024	256	218.7	0.244	0.582	7.788	10.63
2.2×10^6	1	4000	1280	1024	256	266.1	0.138	0.953	8.568	8.848
2.2×10^6	1	6000	2048	1280	256	368.7	0.061	2.021	10.96	7.551
2.2×10^6	1	8000	4096	2048	256	470.0	0.034	3.350	13.44	6.904
2.2×10^6	1	10000	4608	2304	320	575.3	0.022	5.123	16.12	6.619
4.6×10^6	1	0	1280	1024	256	0	∞	0	12.83	∞
4.6×10^6	1	2000	1280	1024	256	193.2	1.150	0.139	9.353	18.66
4.6×10^6	1	3000	1280	1024	256	241.0	0.511	0.316	9.502	12.91
4.6×10^6	1	4000	1280	1024	256	280.4	0.288	0.466	9.626	9.829
4.6×10^6	1	6000	2048	1280	256	383.1	0.128	0.982	11.88	8.154
4.6×10^6	1	8000	4096	2048	256	481.5	0.072	1.644	14.08	7.244
4.6×10^6	1	10000	4608	2304	320	587.7	0.046	2.512	16.76	6.910
1.0×10^7	1	0	1280	1024	256	0	∞	0	16.18	∞
1.0×10^7	1	2000	1280	1024	256	216.5	2.500	0.075	12.41	23.45
1.0×10^7	1	3000	1280	1024	256	269.9	1.111	0.156	12.02	16.19
1.0×10^7	1	4000	1280	1024	256	310.7	0.625	0.233	11.78	12.07
1.0×10^7	1	6000	2048	1280	256	397.3	0.278	0.475	12.85	8.771
1.0×10^7	1	8000	4096	2048	256	501.1	0.156	0.785	15.30	7.848
1.0×10^7	1	10000	6144	3072	320	604.3	0.100	1.218	17.85	7.305
2.2×10^7	1	0	1280	1024	256	0	∞	0	20.92	∞
2.2×10^7	1	2000	1280	1024	256	241.4	5.500	0.036	16.97	29.15
2.2×10^7	1	3000	1280	1024	256	302.9	2.445	0.078	16.13	20.40
2.2×10^7	1	4000	2048	1280	256	351.1	1.375	0.118	15.90	15.42
2.2×10^7	1	6000	3072	1536	256	435.8	0.611	0.243	15.43	10.56
2.2×10^7	1	8000	4096	2048	256	522.0	0.344	0.374	16.52	8.517
2.2×10^7	1	10000	6144	3072	320	613.9	0.220	0.644	18.01	7.541
1.0×10^8	1	0	1280	1024	256	0	∞	0	36.52	∞
1.0×10^8	1	2000	1280	1024	256	307.2	25.00	0.009	35.06	47.20
1.0×10^8	1	3000	2048	1280	256	365.5	11.11	0.014	29.18	29.68
1.0×10^8	1	4000	3072	1536	256	440.6	6.250	0.030	27.23	24.27
1.0×10^8	1	6000	4608	2304	320	557.0	2.778	0.060	26.27	17.24
1.0×10^8	1	8000	6144	3072	320	660.6	1.563	0.097	26.00	13.64
1.0×10^8	1	10000	6912	3456	384	740.2	1.000	0.160	25.21	10.96

TABLE 2. Main simulations considered in this work.

FIGURE 4. Nu as a function of Ra and Re_w in Couette-RB flow.

by the temperature difference between the plates Δ , and P the pressure normalized by $g\beta\Delta/H$.

To solve equations (2.1) - (2.2) we employ the second-order finite difference code AFiD (van der Poel *et al.* 2015), which has been validated many times against other numerical and experimental results (Verzicco & Orlandi 1996; Verzicco & Camussi 1997, 2003; Stevens *et al.* 2010, 2011; Ostilla-Mónico *et al.* 2014; Kooij *et al.* 2018). The code uses periodic boundary conditions with uniform mesh spacing in the horizontal directions and supports a non-uniform grid distribution in the wall-normal direction. For this study we used the GPU version of the code (Zhu *et al.* 2018b) to allow efficient execution of many large-scale simulations. The Couette flow forcing is realized by moving both walls in opposite directions with speed u_w and the results for the pure Couette flow case match excellently with the results by Pirozzoli *et al.* (2014). For example, figure 2b shows that for Couette flow $Re_\tau \sim Re_w^{0.85}$, which agrees very well with the Couette data of Pirozzoli *et al.* (2014) and Avsarkisov *et al.* (2014).

All simulations in this study were performed in a large $9\pi H \times 4\pi H \times H$ box, in stream-wise, spanwise and wall-normal direction (Tsukahara *et al.* 2006; Pirozzoli *et al.* 2014), which is required to capture the large-scale structures formed in the Couette (Pirozzoli *et al.* 2014; Avsarkisov *et al.* 2014; Lee & Moser 2018). We adopted the grid distribution used by Pirozzoli *et al.* (2014, 2017), which is based on the resolution requirements for pure buoyant flow (Shishkina *et al.* 2010) and pure channel flow (Bernardini *et al.* 2014), which is very similar to our flow configuration. As initial condition for our code we use previous flow fields and we make sure that all simulations are statistically stable before extracting data to ensure an independence on the initial conditions. We performed additional simulations with varying grid resolutions as additional grid refinement check for the $Ra = 10^8$ and $Re_w = 10000$ case, i.e. the most challenging simulation of this study. To keep this resolution test manageable it is performed in a smaller $2\pi H \times \pi H \times H$ domain, see table 1. Figure 3 confirms that the simulations are fully resolved for the chosen resolution. As a further validation, we evaluate the Couette data from Pirozzoli *et al.* (2014) in §3.2, which collapses very well with our data. Table 2 shows the simulation parameters for the main cases presented in this study.

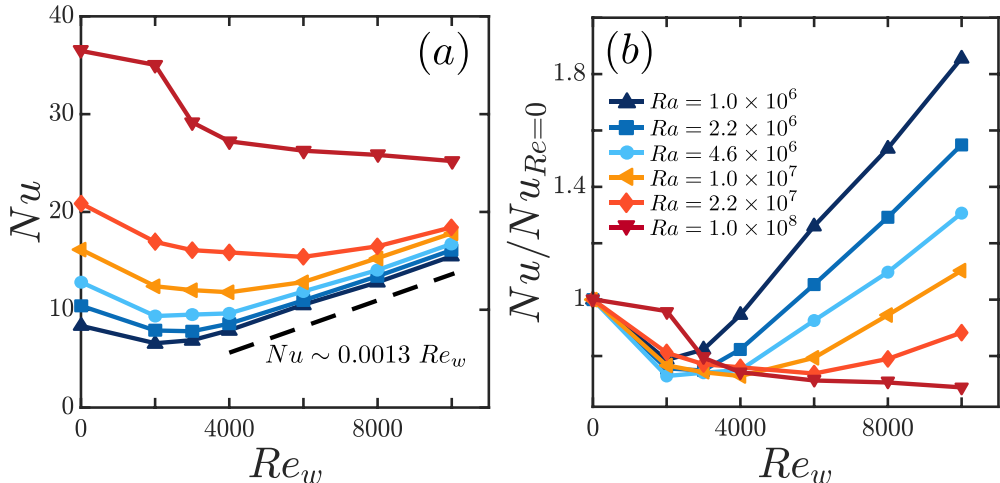


FIGURE 5. (a) Nu and (b) Nu normalized by the RB value $Nu_{(Re_w=0)}$ as a function of Re_w .

3. Global flow characteristics

3.1. Effective scaling of the Nusselt number

Figure 4 shows that the heat transfer increases with increasing Ra and Re_w and that for given Ra number a minimum heat transfer is obtained at some intermediate Re_w . Figure 5a shows the corresponding cross sections for constant Ra which clearly reveal that the location of the minimum heat transfer at constant Ra shifts towards higher Re_w with increasing Ra . For high enough Re_w , the behavior of Nu converges towards $Nu \sim 0.0013 Re_w$. In panel 5b, where Nu is normalized by the RB value for the respective Ra , we can see very clearly that for low Re_w and with increasing Ra the thermal plumes become stronger and therefore harder to disturb by the applied shear. For $Ra = 10^8$ the decrease in Nu at $Re_w = 2000$ is only $\sim 4\%$ while the data for other Ra show percentages in the high twenties. A more exact analysis would need more detailed datapoints for low Re_w .

The results indicate that this mechanism is influenced by the ratio of the buoyancy and shear forces. Therefore the bulk Richardson number Ri or the above defined Monin-Obukhov length L_{MO} , which take the ratio of these forces into account, are natural control and response parameters to identify the different flow regimes. Although the Monin-Obukhov theory itself is only valid for shear dominated flow, which does not necessarily exist in parts of our flow simulations, we use this parameter as an objective criterion to distinct between buoyancy and shear driven flow. As L_{MO} can be compared to other important length scales in the flow, we decide to use it for this purpose. From the data in table 2, we find $L_{MO}/H \approx 0.16/Ri^{0.91}$ (see appendix C). In figure 6a the Monin-Obukhov length is compared to the thermal boundary layer thickness λ_θ and the arbitrary threshold $0.5H$ is reported for later discussion. Since L_{MO}/H is the fraction of the domain in which the shear forcing is dominant in the flow, $L_{MO} \geq 0.5H$ is the threshold from which on the flow is completely shear dominated since the wall generated shear affects at least half of the fluid layer thickness. This allows us to define three different flow regimes, namely a buoyancy dominated regime ($L_{MO} \lesssim \lambda_\theta$), a transitional regime ($0.5H \gtrsim L_{MO} \gtrsim \lambda_\theta$), and a shear dominated regime ($L_{MO} \gtrsim 0.5H$). A similar behavior has also been observed in convective boundary layers, where Salesky *et al.* (2017) find a cell dominated regime for $z_i/L_{MO} > 20$, where z_i is the convective boundary layer

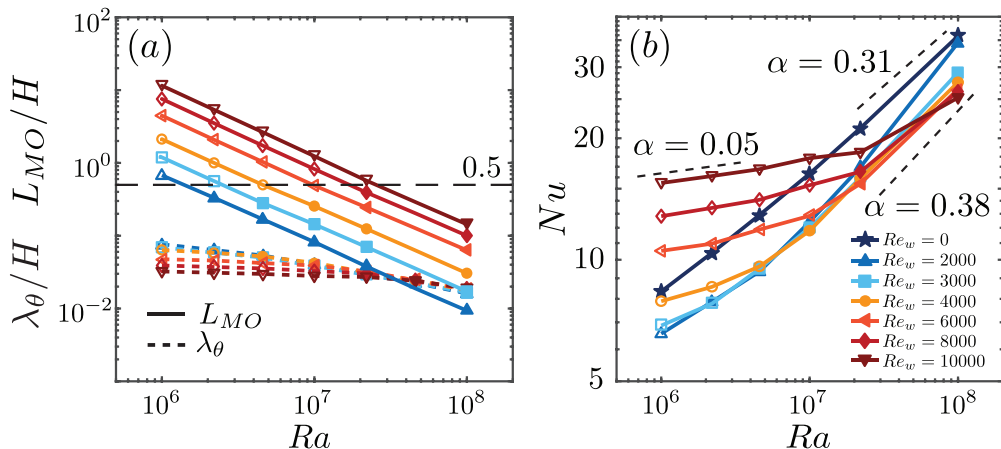


FIGURE 6. (a) The Monin-Obukhov length L_{MO} as function of Ra for different Re_w . L_{MO} is compared to the thermal boundary layer thickness λ_θ and $0.5H$ to define the flow regime (temperature dominated, transition, shear dominant) of each simulations, see details in the text. (b) Nu as function of Ra . The numbers indicate the scaling exponent α in $Nu \sim Ra^\alpha$.

thickness, a cell and roll dominated regime as transitional state, and a roll dominated regime for $z_i/L_{MO} < 5$.

Figure 6b shows that the heat transfer in the buoyancy dominated regime scales as $Nu \sim Ra^{0.31}$, as also found for classical RB convection ($Re_w = 0$, Ahlers *et al.* (2009)). For the shear dominated regime we find that the effective scaling exponent α in $Nu \sim Ra^\alpha$ is $\alpha \ll 1/3$ and in the transitional regime we find $\alpha > 1/3$. An effective scaling exponent larger than $1/3$ is one of the characteristics of the ultimate regime. It should occur when the boundary layers have transitioned to the turbulent state, which is indicated by their logarithmic profiles. Our analysis in §4 will show that this is not yet the case in this transitional regime. Instead, for intermediate shear, the heat transfer is decreased with respect to the RB case. The locally larger effective scaling exponent simply is a consequence of the fact that with increasing Ra the heat transfer, which was decreased at intermediate shear, must again converge to the RB case.

3.2. Skin Friction

In figure 7 we compare the measured skin friction coefficient for different Re_w and Ra with Prandtl's turbulent friction law (Schlichting & Gersten 2000):

$$\sqrt{\frac{2}{C_f}} = \frac{1}{\mathcal{K}} \log \left(Re_w \sqrt{\frac{C_f}{2}} \right) + C. \quad (3.1)$$

Following Pirozzoli *et al.* (2014) we use a von Kármán constant $\mathcal{K} = 0.41$ and $C = 5$. The figure shows that the skin friction increases with Ra and decreases with Re_w . At fixed Ra the relative strength of the thermal forcing decreases for high Re_w and therefore the obtained friction coefficient converges to the Prandtl law. This agrees very well with Scagliarini *et al.* (2015) and Pirozzoli *et al.* (2017) for buoyant Poiseuille flow. In figure 7b we focus on the data for small Re_w . The skin friction in pure Couette flow follows the expected laminar result $C_f = 4/Re_w$ (Pope 2000) until a transition to the turbulent state occurs around $Re_w = 650 - 700$. Cerbus *et al.* (2018) discuss that in pipe flow this jump is caused by the formation of puffs and slugs. Brethouwer *et al.* (2012) attribute this discontinuous jump in C_f to the lack of restoring forces in plane Couette flow (similar

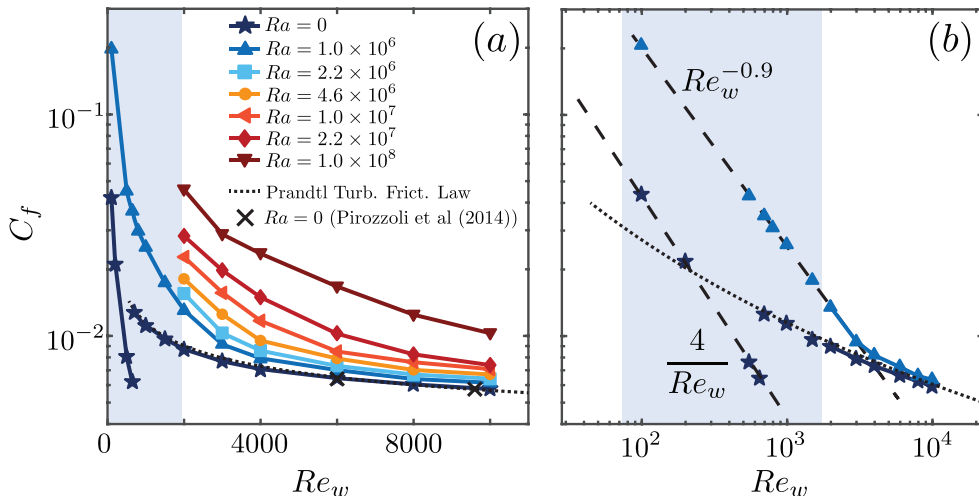


FIGURE 7. (a) Skin friction coefficient C_f as a function of Re_w . (b) Zoom-in of the gray area shown in panel (a), now on a log-scale, showing the data for pure Couette flow ($Ra = 0$, stars) and $Ra = 10^6$. Note that $C_f(Ra = 0)$ follows the expected laminar result (---) until $Re_w = 650 - 700$ and then jumps to the turbulent curve (···). For Couette-RB, i.e. the uppointing triangle, no jump is observed.

to pipe, channel and boundary layer flows). For the Couette-RB case we do not observe such a discontinuous jump. Instead this sheared RB case is another example, next to the application of Coriolis, buoyancy, and Lorentz forces discussed by Brethouwer *et al.* (2012), which shows that restoring forces can prevent a discontinuous jump in $C_f(Re_w)$. Chantry *et al.* (2017), on the other hand, claim that all transitions to turbulence should be continuous if the used box size is large enough. From this figure we can also judge whether a boundary layer is turbulent or not. When the slope of C_f approaches the one of pure Couette flow, the boundary layers are turbulent. Once this slope starts to strongly deviate from the Prandtl law, we consider the boundary layer as not turbulent.

4. Local flow characteristics

4.1. Organization of turbulent structures

To further investigate the dynamics of the different regimes, we show visualizations of the temperature field for all simulations in figure 8 and Appendix A. We chose the mid-height for the location of these two-dimensional snapshots, since this is the position where the flow is the least affected by the wall. In the thermally dominated regime the primary flow structure resembles the large-scale flow found in RB convection (Stevens *et al.* 2018). In the transitional regime ($L_{MO} \lesssim 0.5H$), the thermal forcing dominates part of the bulk where large elongated thermal plumes transform into thin straight elongated streaks when L_{MO} approaches $0.5H$. In figure 8 and in the appendix this manifests itself as a very visual line diagonally through the diagram, splitting the more thermal- and the more shear dominated cases. In the shear dominated regime ($L_{MO} \gtrsim 0.5H$) we find large-scale meandering structures, similar to the ones found in pressure-driven channel flow with unstable stratification (Pirozzoli *et al.* 2017). This significant change in flow structure can be linked to the minimum in Nu in figure 5. The reason for the minimum is that at intermediate shear the thermal convection rolls are broken up, while the shear is not yet strong enough to increase the heat transfer directly. This observation is in agreement

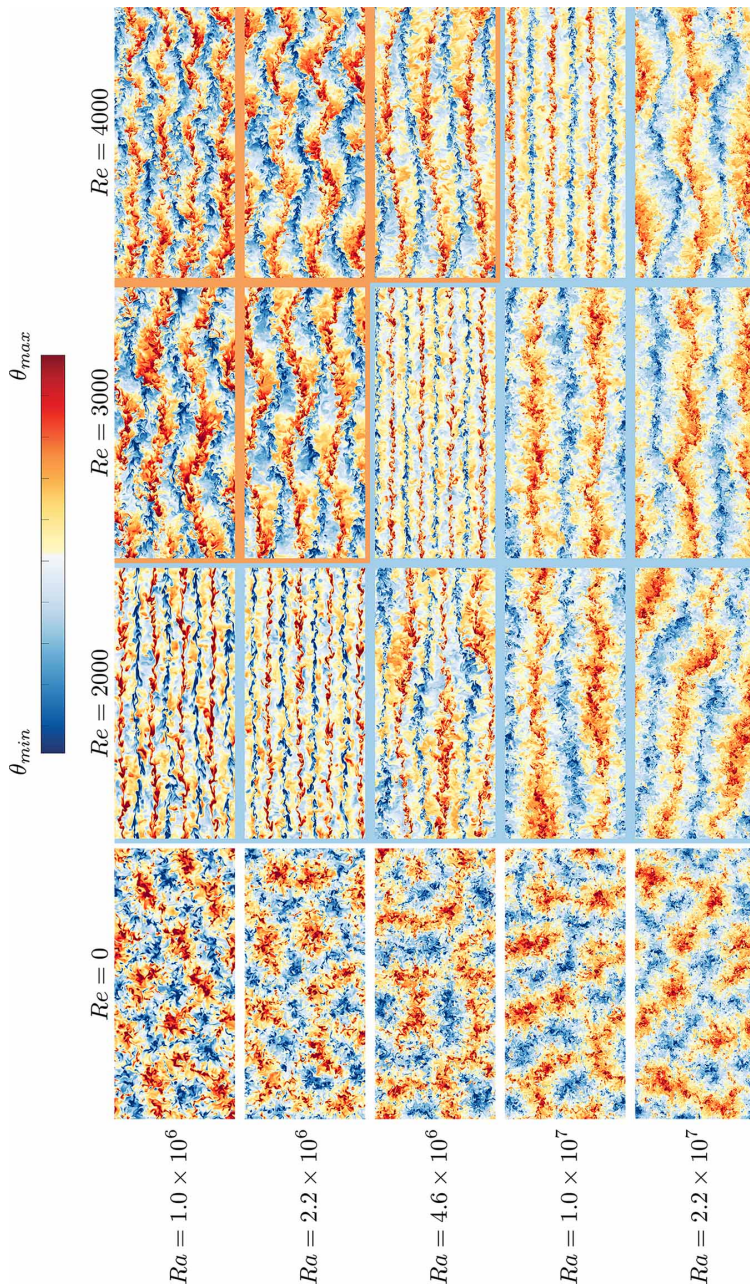


FIGURE 8. Instantaneous snapshots of temperature fields at midheight for a subdomain of the parameter space, see figure 2a and table 1, focusing on $Ra = 1.0 \times 10^6 - 2.2 \times 10^7$ and $Re_w = 0 - 4000$. The panels have colored borders depending on the flow regime they display: thermal dominated (white), transitional (blue), and shear dominated (orange) regime. For a more detailed quantification of the different flow fields in the presented snapshots, we would like to refer to the values for the Monin-Obukhov length L_{MO} in table 2. An overview of temperature fields over the whole domain can be found in appendix A. The color ranges of the snapshots in this figure and in figures 9, 10, 11, and 14 are defined as a variable temperature range for each subfigure to better display the behavior of the thermal structures while keeping the coloring of the structures similar.

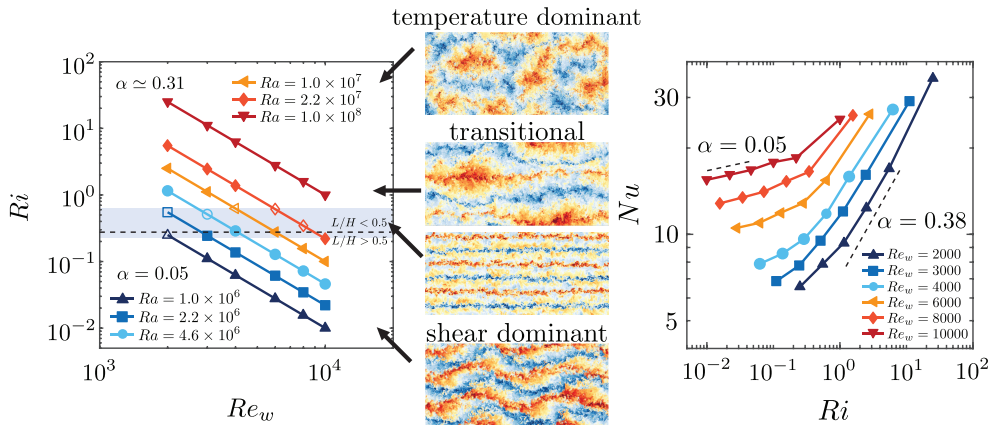


FIGURE 9. Left: Ri versus Re_w for different Ra . Open symbols indicate the presence of thin straight elongated streaks (see third snapshot from top). The dashed line indicates $L_{MO} = 0.5H$. In the middle: instantaneous snapshots of temperature fields at midheight. Right: Nu as a function of Ri for different Re_w . An indication of the effective scaling exponent α in $Nu \sim Ra^\alpha$ in the different regimes is also given. For a more detailed quantification of the different flow regimes in the presented snapshots, we would like to refer to the values for the Monin-Obukhov length L_{MO} in table 2.

with earlier works described above (Domaradzki & Metcalfe 1988; Scagliarini *et al.* 2014, 2015; Pirozzoli *et al.* 2017).

In figure 9 we want to present a clear overview over the behavior of the flow structures versus the flow control parameters combined in the bulk Richardson number. On the left side we compare the different values of Ri with the visually observed flow structures. We find a range of Ri in which the flow undergoes a change from the transitional to the shear dominated regime. This happens in a range of $0.2 \lesssim Ri \lesssim 0.7$. In the right panel we can also detect this trend, where the effective scaling of the Nusselt number changes from $Nu \sim Ri^{0.05}$ to $Nu \sim Ri^{0.38}$, but more data points would be necessary to define a more exact point of transition.

Figure 9 combines these findings with the above observation that in the shear dominated regime the effective scaling exponent α in $Nu \sim Ra^\alpha$ is much smaller than $1/3$, in the transitional regime $\alpha > 1/3$, and in the thermally dominated regime $\alpha \simeq 0.31$. When we compare the regime transitions with the results in figure 5, it becomes clear that the lowest heat transfer for a given Ra occurs at the end of the transitional regime just before the emergence of the thin straight elongated streaks. Due to the large computational time that is required for each simulation the number of considered cases is limited, which makes it difficult to pinpoint exactly when the heat transfer is minimal and what the flow structure looks like in that case. However, we note that the onset of the shear dominant regime corresponds to the point where the heat transfer starts to increase as the additional shear can then more effectively enhance the overall heat transport.

To get more insight into the boundary layer dynamics in the different regimes, we show the temperature and streamwise velocity at boundary layer height for $Ra = 4.6 \times 10^6$ in figure 10. At this Rayleigh the flow is in the transitional regime for $Re_w = 2000$ and $Re_w = 3000$, and in the shear dominant regime for $Re_w \geq 4000$. For all cases we observe a clear imprint of the large-scale structures observed at midheight, see figure 8 and Appendix A. This indicates that the large-scale dynamics have a pronounced influence on the flow structures in the boundary layers (Stevens *et al.* 2018). The figure also reveals that in the transitional and shear dominated regime the lowest temperatures

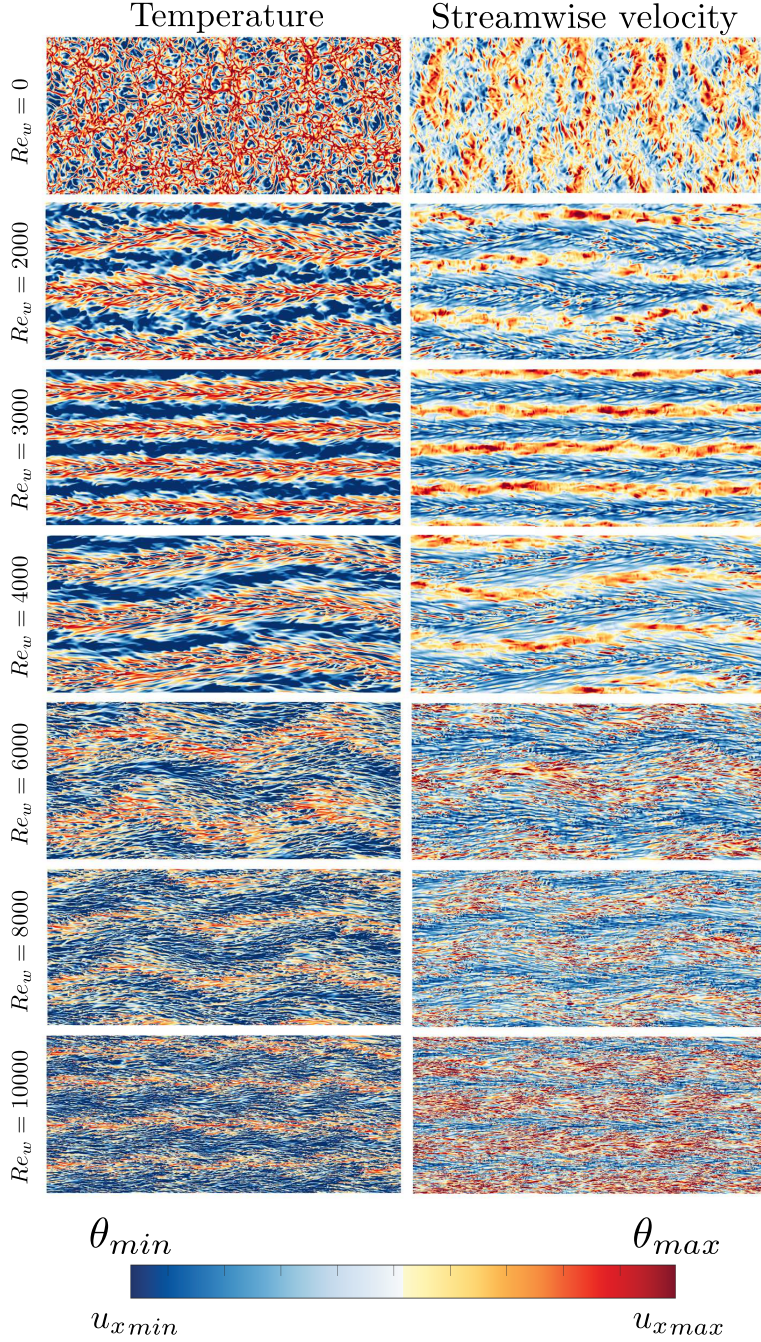


FIGURE 10. Instantaneous near-wall snapshots at $z^+ \approx 0.5$ of the temperature (left) and streamwise velocity (right) for $Ra = 4.6 \times 10^6$. Re_w increases from top to bottom. For a more detailed quantification of the different flow fields in the presented snapshots, we would like to refer to the values for the Monin-Obukhov length L_{MO} in table 2.

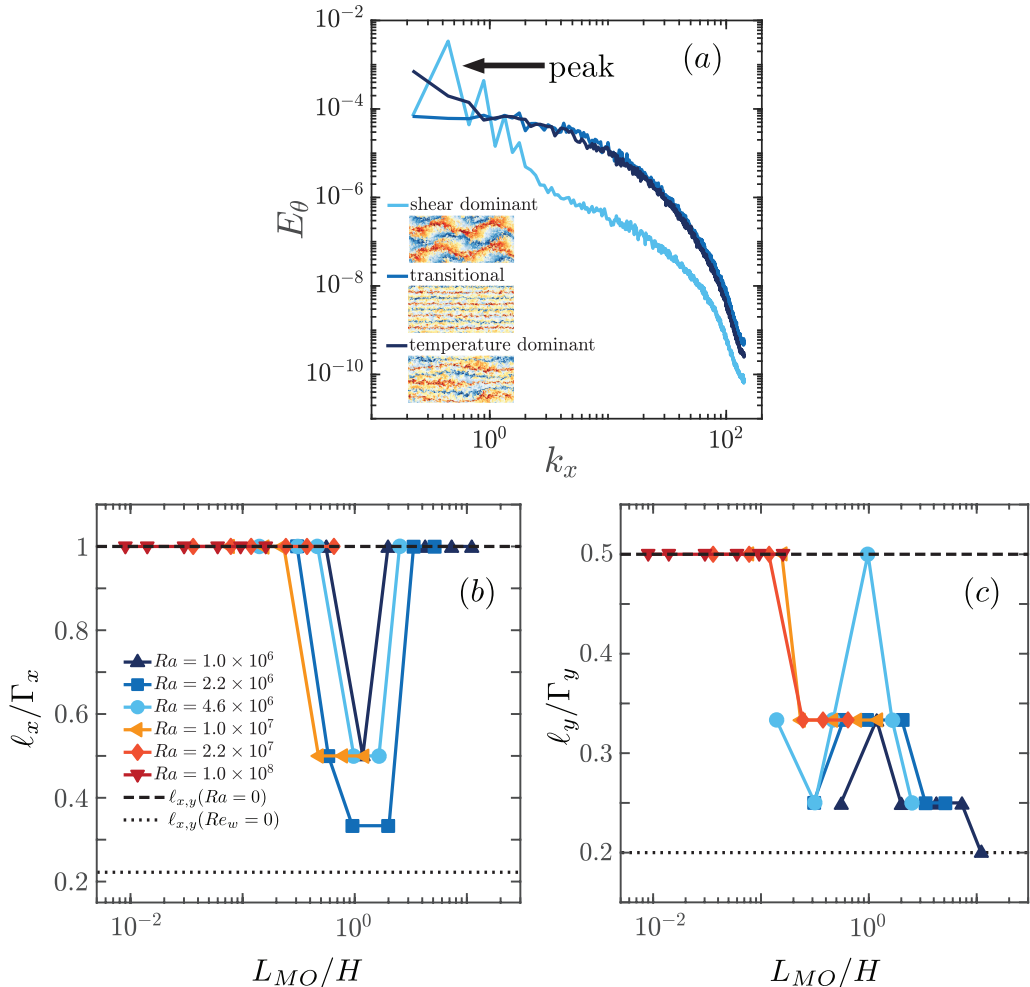


FIGURE 11. (a) Overview over streamwise temperature variance spectra at $Ra = 4.6 \times 10^6$ for different flow regimes at midheight, (b,c) evolution of peaks in streamwise and spanwise temperature variance spectra, respectively, versus the Monin-Obukhov length.

at boundary layer height are observed in the high speed streak regions, which indicates that the regions with the highest shear contribute most to the overall heat flux.

4.2. Flow statistics

We now present the streamwise temperature variance spectra $E_\theta(k)$ in figure 11 to analyse the size of the large-scale structures as function of the Monin-Obukhov length. The position of the peak in the temperature spectrum indicates the wavelength of the most prominent thermal structure (Stevens *et al.* 2018). In panel (b) and (c) we plot the evolution of the wavelength of these structures in relation to the absolute size of the flow field. Therefore we define $k_{x_{peak}}$ and $k_{y_{peak}}$ as the wavenumbers of the peak in the respective energy spectrum and $\ell_x = 2\pi/k_{x_{peak}}$ and $\ell_y = 2\pi/k_{y_{peak}}$ as the respective wavelengths. If the spectrum does not show a clear peak, but keeps growing for small k , the structure size is set to the limits of the simulation box, which is $\Gamma_x = 9\pi$ in streamwise (figure 11b) and $\Gamma_y = 4\pi$ in spanwise direction (figure 11c) in this manuscript.

For $L_{MO} \rightarrow \infty$, $\ell_x \approx \Gamma_x H$, which is expected since for pure Couette flow, structures

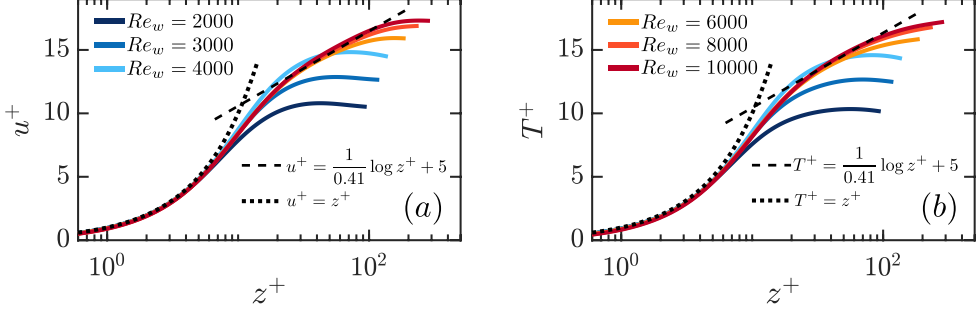


FIGURE 12. (a) Mean streamwise velocity and (b) temperature profiles, where $u^+ = u/u_\tau$ and, following Pirozzoli *et al.* (2017), $T^+ = T/T_\tau$ with the friction temperature $T_\tau = Q/u_\tau$ for $Ra = 4.6 \times 10^6$.

much larger than 9π are expected (Lee & Moser 2018). $\ell_y \approx 0.8\pi H = 0.2\Gamma_y H$ for the highest shear case, but here more data points are needed for a clearer determination of its behavior. In the other limit of $L_{MO} \rightarrow 0$, i.e. in the transitional regime as the RB case (buoyancy dominated regime) is not shown due to the logarithmic axis, the large-scale structures are elongated over the whole streamwise length, which is consistent with figure 8 and figure 14. For pure RB convection, where $L_{MO} = 0$, ℓ_x decreases to $\ell_x \approx 2\pi H$ and is in agreement with Stevens *et al.* (2018). In the spanwise direction, the flow converges already much earlier to the RB case where $\ell_y \approx 2\pi H = 0.5\Gamma_y H$.

In the shear dominated regime, where the flow meanders, the structure size in streamwise direction drops to about half the box length. In spanwise direction this flow regime is present as a local peak in panel (c). Due to the very limited number of datapoints, it is not possible to fully assess the behavior of ℓ_x and ℓ_y vs L_{MO} for all Ra and Re_w . Nevertheless the minimum in ℓ_x and peak in ℓ_y in the shear dominated regime are very distinct.

To further quantify the cases shown in figure 10, we study their flow statistics in figure 12. It becomes clear that both the temperature and streamwise velocity profiles are not logarithmic in the transitional regime. This indicates that the boundary layers are not turbulent in this state. Hence, the higher Nu scaling in the transitional regime does not seem to be caused by triggering the ultimate regime. In the shear dominated regime the streamwise velocity and temperature profiles seem to converge to a logarithmic profile with increasing Re_w which has also been previously observed in Couette flow (Liu 2003; Debusschere & Rutland 2004; Choi *et al.* 2004; Le & Papavassiliou 2006) and Poiseuille flow (Scagliarini *et al.* 2015; Pirozzoli *et al.* 2017) with convection.

In figure 13 we show the same statistical quantities as in figure 12, but now for fixed $Re_w = 6000$. For $Ra \gtrsim 10^7$ the flow is in the transitional regime and for $Ra \lesssim 10^7$ the flow undergoes a transition into the shear dominated regime. Just as in figure 12 we observe that the temperature and streamwise velocity profiles are not logarithmic in the transitional regime. As the Richardson number decreases with decreasing Ra , we see that the profiles converge towards a logarithmic behavior. From a comparison with table 2 we find that $Ri \lesssim 0.2$ seems to be required to achieve logarithmic temperature and velocity profiles. If we refer back to figure 9, we can confirm that $Ri \approx 0.2$ is indeed the threshold where the flow undergoes its transition to the shear dominated regime. This is also consistent with the work of Pirozzoli *et al.* (2017), who report a regime with increased importance of friction at $Ri \approx 0.1$. For the parameter regime under investigation the effective scaling exponent α in this regime is well below $1/3$. In both figures we can detect a non-monotonic behavior of both u^+ and T^+ for low Re_w and high Ra . This is

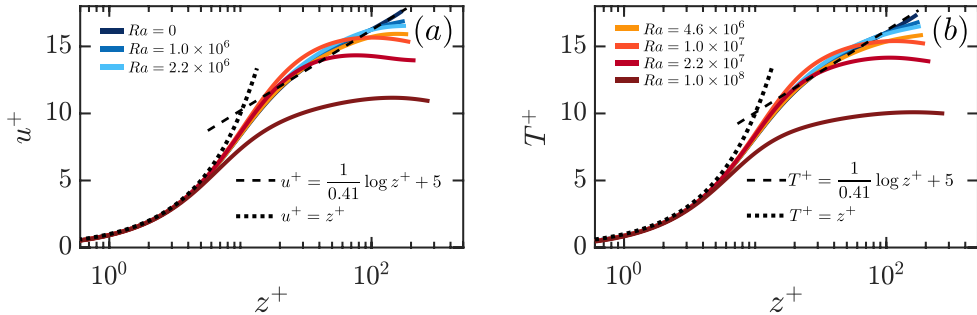


FIGURE 13. (a) Mean streamwise velocity and (b) temperature profiles, where $u^+ = u/u_\tau$ and $T^+ = T/T_\tau$ with $T_\tau = Q/u_\tau$ for $Re_w = 6000$. $T^+_{Ra=0}$ was determined through a passive-scalar temperature field.

connected to an effect of flow layering in the transitional regime where the large-scale thermal plumes get distorted by the shear, but not enough for the meandering structures to evolve and break up this effect. Several further statistical quantities for both constant Ra and constant Re_w have been calculated and can be found in appendix B.

5. Concluding remarks

We performed direct numerical simulations of turbulent thermal convection with Couette type flow shearing. We presented cases in a range $10^6 \leq Ra \leq 10^8$ and $0 \leq Re_w \leq 10^4$, achieving up to $Re_\tau \approx 740$. For fixed Rayleigh number we obtain a non-monotonic progression of Nu similarly to what was previously observed in unstable stratification with a pressure gradient (Scagliarini *et al.* 2014). The addition of imposed shear to thermal convection first leads to a reduction of the heat transport by disrupting the turbulent system before the shear becomes strong enough to create meandering streaks that efficiently transport the heat away from the wall. As the impact of the thermal plumes on the flow decreases with increasing shear, the skin friction coefficient at constant Ra drops with increasing Re_w .

We find that three flow regimes can be identified in Couette-RB using the Monin-Obukhov length L_{MO} and the thermal boundary layer thickness λ_θ . In the buoyancy dominated regime ($L_{MO} \lesssim \lambda_\theta$) the flow is dominated by large thermal plumes. With decreasing Richardson number we first find a transitional regime ($0.5H \gtrsim L_{MO} \gtrsim \lambda_\theta$), before the shear dominated flow regime with large-scale meandering streaks is obtained. For a given Ra the minimum heat transport is found just before the onset of this shear dominated regime when thin straight elongated streaks dominate the flow. We find that in the transitional regime the effective scaling exponent α in $Nu \sim Ra^\alpha$ is larger than $1/3$. An analysis of the flow characteristics shows that the temperature and streamwise velocity profiles are not logarithmic in this transitional regime, which one would expect when this high scaling exponent would indicate the onset of the ultimate regime. Since it is possible to recover logarithmic profiles for low Richardson number flows we want to investigate in future studies whether it is possible to increase the thermal and sheared forcing far enough to trigger ultimate convection in Couette-RB.

Acknowledgments

We thank Colm-Cille Caulfield and Daniel Chung for fruitful discussions and Jean M. Favre for his support with three-dimensional data visualizations which resulted in figure

1. The simulations were supported by a grant from the Swiss National Supercomputing Centre (CSCS) under project ID s713, s802, and s874. This work was financially supported by NWO, by the Dutch center for Multiscale Catalytic Energy Conversion (MCEC), the ERC Advanced Grant “Diffusive Droplet Dynamics in multicomponent fluid systems”, and the Priority Programme SPP 1881 “Turbulent Superstructures” of the Deutsche Forschungsgemeinschaft. We also acknowledge the Dutch national e-infrastructure SURFsara with the support of SURF cooperative.

Appendix A. Flow Field Overview

As an addition to figure 8 we present here in figure 14 the full overview of all temperature fields at midheight, ranging from $Ra = 1.0 \times 10^6 - 1.0 \times 10^8$ and $Re_w = 0 - 10000$. All three regimes of thermal domination, transition, and shear domination can be observed here.

Appendix B. Further Flow Statistics

Additionally to figures 12 and 13 we present further flow statistics in this section. Figure 15 shows the statistical behavior of the flow for constant $Ra = 4.6 \times 10^6$ and increasing wall shearing. It can be observed that the velocity fluctuations increase with Re_w . The peaks of the temperature fluctuations show a non-monotonic behavior. For low shearing, they first increase with Re_w until it undergoes a transition towards the shear dominated regime, where the temperature fluctuations decrease with increasing wall shearing.

In figure 16 we present the same flow statistics for constant $Re_w = 6000$ and increasing thermal forcing, starting at plane Couette flow ($Ra = 0$). When thermal forcing is added to the Couette flow u_{peak} and v_{peak} first increase and then monotonically decrease for increasing Ra . Both the wall-normal velocity and the temperature fluctuations decrease completely monotonic for increasing thermal forcing.

Appendix C. Monin-Obukhov Fitting

In figure 17 we present the ratio of shear and thermal forcing in form of the flow output parameter L_{MO}/H versus the flow input parameter Ri from all datapoints of our simulations. We find that the Monin-Obukhov length scales as $L_{MO}/H = 0.16/Ri^{0.91}$.

Appendix D. Comparison of L_{MO} and λ_θ

In addition to figure 6a we present a further visualization of the Monin-Obukhov scale in figure 18, here normalized by the thermal boundary layer thickness λ_θ . For $L_{MO}/\lambda_\theta < 1$ the flow is in the thermally dominated regime. For higher L_{MO}/λ_θ , the flow first reaches the transitional regime before the shear dominated regime is reached, where $L_{MO}/\lambda_\theta \sim Re_w^{5/2}$.

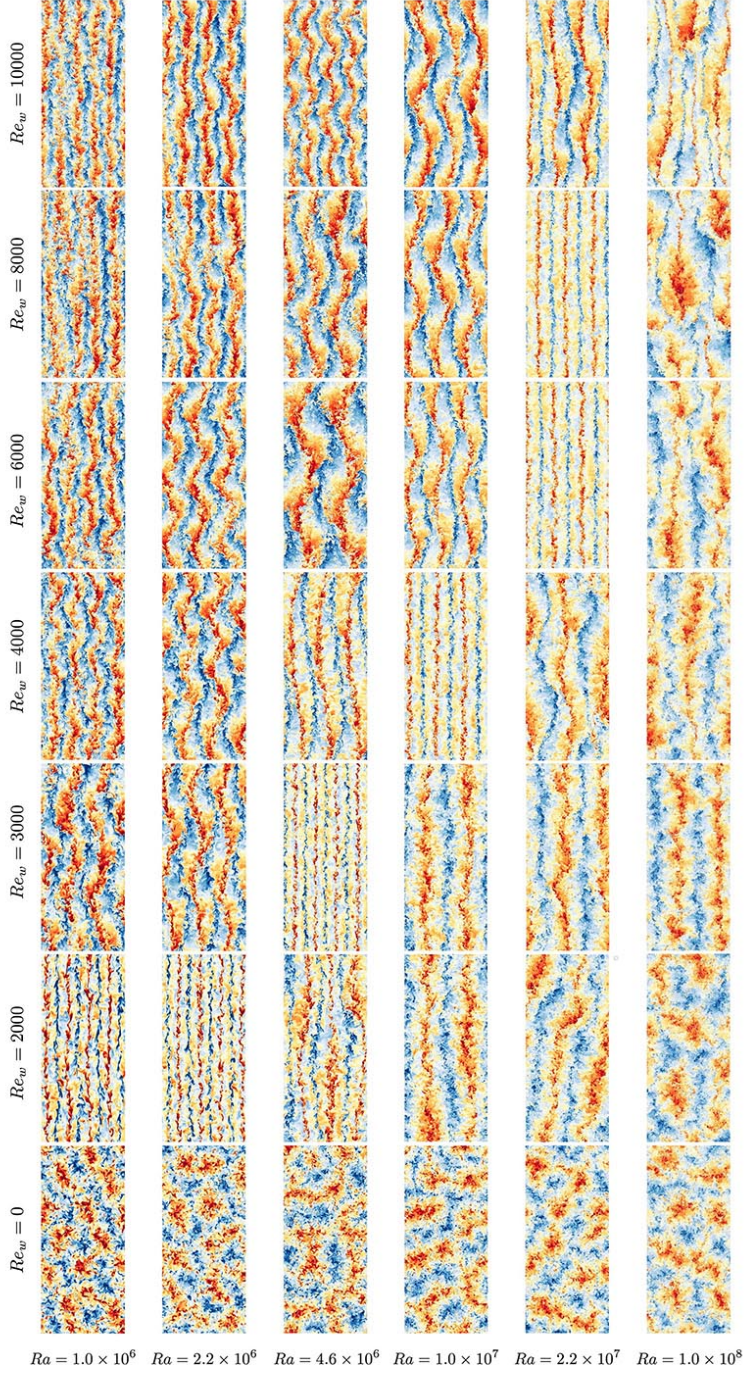


FIGURE 14. Instantaneous snapshots of all simulated temperature fields at midheight.

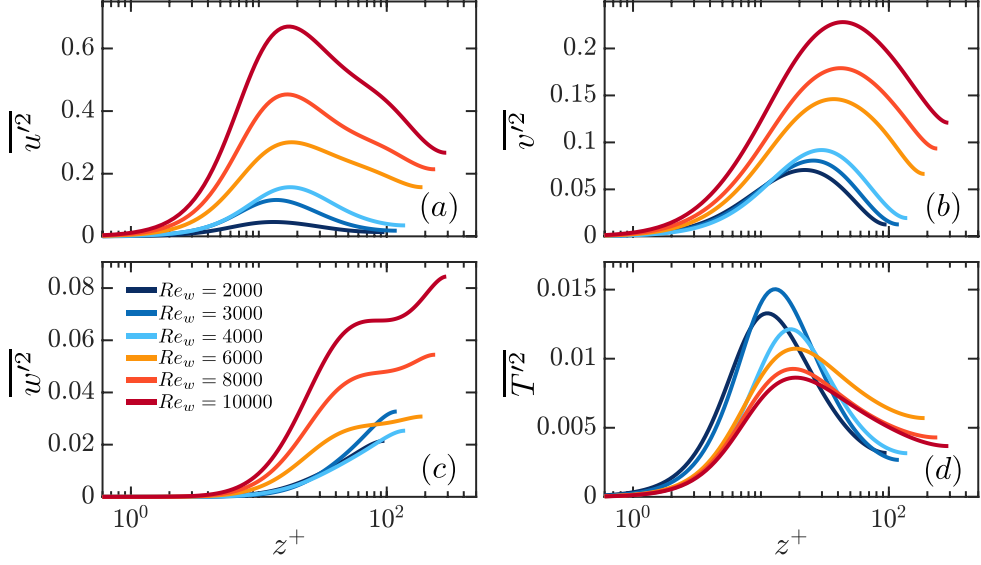


FIGURE 15. Fluctuations of (a) streamwise, (b) spanwise velocity, (c) wall-normal velocity, and (d) temperature for $Ra = 4.6 \times 10^6$ in wall units.

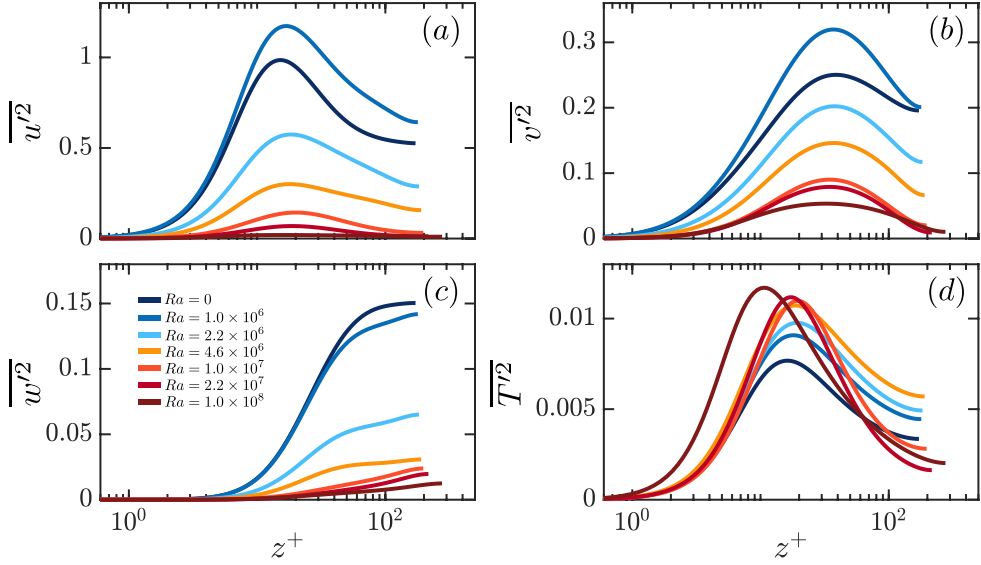


FIGURE 16. Fluctuations of (a) streamwise, (b) spanwise velocity, (c) wall-normal velocity, and (d) temperature for $Re_w = 6000$ in wall units. $\overline{T'^2}_{Ra=0}$ was determined through a passive-scalar temperature field.

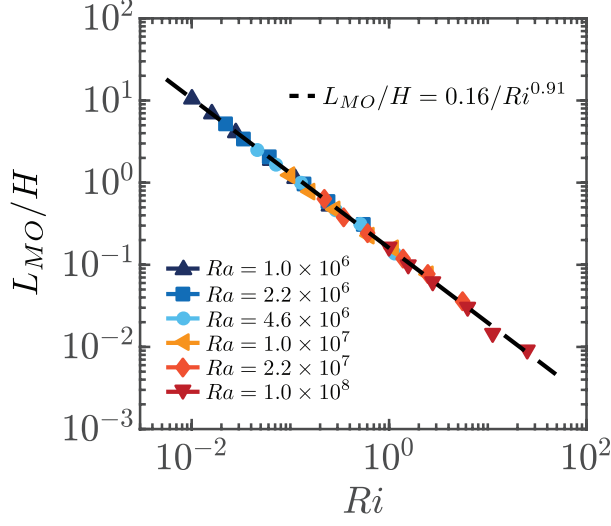


FIGURE 17. L_{MO}/H versus Ri of DNS datapoints and the fit $L_{MO}/H = 0.16/Ri^{0.91}$.

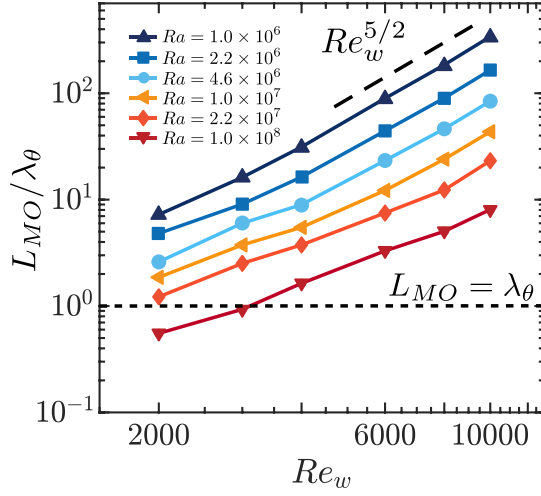


FIGURE 18. L_{MO} normalized by the thermal boundary layer thickness λ_θ versus Re_w . For $L_{MO}/\lambda_\theta < 1$ the flow is in the thermally dominated regime.

REFERENCES

- AHLERS, G., GROSSMANN, S. & LOHSE, D. 2009 Heat transfer and large scale dynamics in turbulent Rayleigh-Bénard convection. *Rev. Mod. Phys.* **81**, 503.
- AHLERS, G., HE, X., FUNFSCHILLING, D. & BODENSCHATZ, E. 2012 Heat transport by turbulent Rayleigh-Bénard convection for $Pr = 0.8$ and $3 \times 10^{12} < Ra < 10^{15}$: aspect ratio $\Gamma = 0.50$. *New J. Phys.* **14**, 103012.
- AVSARKISOV, V., HOYAS, S. & GARCÍA-GALACHE, M. OBERLACK J. P. 2014 Turbulent plane Couette flow at moderately high Reynolds number. *J. Fluid Mech.* **751**.
- BARKLEY, D. & TUCKERMAN, L. S. 2005 Computational study of turbulent laminar patterns in Couette flow. *Phys. Rev. Lett.* **94** (1), 014502.
- BERNARDINI, M., PIROZZOLI, S. & ORLANDI, P. 2014 Velocity statistics in turbulent channel flow up to $re_\tau = 4000$. *J. Fluid Mech.* **742**, 171–191.
- BRETHOUWER, G., DUGUET, Y. & SCHLATTER, P. 2012 Turbulent-laminar coexistence in wall flows with Coriolis, buoyancy or Lorentz forces. *J. Fluid Mech.* **704**, 137–172.
- CERBUS, R.T., LIU, C., GIOIA, G. & CHAKRABORTY, P. 2018 Laws of resistance in transitional pipe flows. *Phys. Rev. Lett.* **120**, 054502.
- CHANTRY, M., TUCKERMAN, L. S. & BARKLEY, D. 2017 Universal continuous transition to turbulence in a planar shear flow. *J. Fluid Mech.* **824**, R1.
- CHILLA, F. & SCHUMACHER, J. 2012 New perspectives in turbulent Rayleigh-Bénard convection. *Eur. Phys. J. E* **35**, 58.
- CHOI, C. K., CHUNG, T. J. & KIM, M. C. 2004 Buoyancy effects in plane Couette flow heated uniformly from below with constant heat flux. *Int. J. Heat Mass Transf.* **47**, 2629–2636.
- CHOLEMARI, M. R. & ARAKERI, J. H. 2009 Axially homogeneous, zero-mean flow buoyancy driven turbulence in a vertical pipe. *J. Fluid Mech.* **621**, 69–102.
- DEARDORFF, J. W. 1972 Numerical investigation of neutral and unstable planetary boundary layers. *J. Atmos. Sci.* **29** (1), 91–115.
- DEBUSSCHERE, B. & RUTLAND, C. J. 2004 Turbulent scalar transport mechanisms in plane channel and Couette flows. *Int. J. Heat Mass Transf.* **47**, 1771–1781.
- DOMARADZKI, J. A. & METCALFE, R. W. 1988 Direct numerical simulations of the effects of shear on turbulent Rayleigh-Bénard convection. *J. Fluid Mech.* **193**, 499.
- FAVRE, J. M. & BLASS, A. 2019 A comparative evaluation of three volume rendering libraries for the visualization of sheared thermal convection. *Parallel Comput.* **88**, 102543.
- FUKUI, K. & NAKAJIMA, M. 1985 Unstable stratification effects on turbulent shear flow in the wall region. *Int. J. Heat Mass Transf.* **28**, 2343–2352.
- GIBERT, M., PABIOU, H., CHILLA, F. & CASTAING, B. 2006 High-Rayleigh-number convection in a vertical channel. *Phys. Rev. Lett.* **96**, 084501.
- GROSSMANN, S. & LOHSE, D. 2000 Scaling in thermal convection: A unifying view. *J. Fluid Mech.* **407**, 27–56.
- GROSSMANN, S. & LOHSE, D. 2001 Thermal convection for large Prandtl number. *Phys. Rev. Lett.* **86**, 3316–3319.
- GROSSMANN, S. & LOHSE, D. 2011 Multiple scaling in the ultimate regime of thermal convection. *Phys. Fluids* **23**, 045108.
- GROSSMANN, S., LOHSE, D. & SUN, C. 2016 High Reynolds number Taylor-Couette turbulence. *Annu. Rev. Fluid Mech.* **48**, 53–80.
- HATHAWAY, D. & SOMERVILLE, R. 1986 Nonlinear interactions between convection, rotation and flows with vertical shear. *J. Fluid Mech.* **164**, 91–105.
- INGERSOLL, A. P. 1966 Thermal convection with shear at high Rayleigh number. *J. Fluid Mech.* **25**, 209.
- JIMÉNEZ, J. 2018 Coherent structures in wall-bounded turbulence. *J. Fluid Mech.* **842**, P1.
- KHANNA, S. & BRASSEUR, J. G. 1998 Three-dimensional buoyancy- and shear-induced local structure of the atmospheric boundary layer. *J. Atmos. Sci.* **55** (5), 710–743.
- KITOH, O. & UMEKI, M. 2008 Experimental study on large-scale streak structure in the core region of turbulent plane Couette flow. *Phys. Fluids* **20**, 025107.
- KOOLJ, G. L., BOTCHEV, M. A., FREDERIX, E. M. A., GEURTS, B. J., HORN, S., LOHSE, D., VAN DER POEL, E. P., SHISHKINA, O., STEVENS, R. J. A. M. & VERZICCO, R.

- 2018 Comparison of computational codes for direct numerical simulations of turbulent Rayleigh-Bénard convection. *Computers & Fluids* **166**, 1–8.
- KRAICHNAN, R. H. 1962 Turbulent thermal convection at arbitrary Prandtl number. *Phys. Fluids* **5**, 1374–1389.
- LE, P. M. & PAPAVALIOU, D. V. 2006 Turbulent heat transfer in plane Couette flow. *J. Heat Transfer* **128**, 53–62.
- LEE, M. & MOSER, R. D. 2018 Extreme-scale motions in turbulent plane couette flows. *J. Fluid Mech.* **842**, 128–145.
- LEE, M. J. & KIM, J. 1991 The structure of turbulence in a simulated plane Couette flow. *Proceedings of the 8th Symposium on Turbulent Shear Flows, Munich* pp. 5.3.1–5.3.6.
- LIU, C. H. 2003 Turbulent plane Couette flow and scalar transport at low Reynolds number. *J. Heat Transfer* **125**, 988–998.
- LOHSE, D. & XIA, K.-Q. 2010 Small-scale properties of turbulent Rayleigh-Bénard convection. *Annu. Rev. Fluid Mech.* **42**, 335–364.
- MOENG, C.-H. 1984 A large-eddy-simulation model for the study of planetary boundary-layer turbulence. *J. Atmos. Sci.* **41** (13), 2052–2062.
- MONIN, A. S. & OBUKHOV, A. M. 1954 Basic laws of turbulent mixing in the surface layer of the atmosphere. *Contrib. Geophys. Inst. Acad. Sci. UDSSR* **151**, 163–187.
- OBUKHOV, A. M. 1971 Turbulence in an atmosphere with a non-uniform temperature. *Bound.-Layer Meteorol.* **2**, 7–29.
- ORLANDI, P., BERNARDINI, M. & PIROZZOLI, S. 2015 Poiseuille and Couette flows in the transitional and fully turbulent regime. *J. Fluid Mech.* **770**, 424–441.
- OSTILLA-MÓNICO, R., VAN DER POEL, E. P., VERZICCO, R., GROSSMANN, S. & LOHSE, D. 2014 Exploring the phase diagram of fully turbulent Taylor-Couette flow. *J. Fluid Mech.* **761**, 1–26.
- PAWAR, S. S. & ARAKERI, J. H. 2016 Two regimes of flux scaling in axially homogeneous turbulent convection in vertical tube. *Phys. Rev. Fluids* **1** (4), 042401.
- PIROZZOLI, S., BERNARDINI, M. & ORLANDI, P. 2011 Large-scale motions and inner/outer layer interactions in turbulent Couette-Poiseuille flows. *J. Fluid Mech.* **680**, 534–563.
- PIROZZOLI, S., BERNARDINI, M. & ORLANDI, P. 2014 Turbulence statistics in Couette flow at high Reynolds number. *J. Fluid Mech.* **758**, 327–343.
- PIROZZOLI, S., BERNARDINI, M., VERZICCO, R. & ORLANDI, P. 2017 Mixed convection in turbulent channels with unstable stratification. *J. Fluid Mech.* **821**, 482–516.
- VAN DER POEL, E. P., OSTILLA-MÓNICO, R., DONNERS, J. & VERZICCO, R. 2015 A pencil distributed finite difference code for strongly turbulent wall-bounded flows. *Computers & Fluids* **116**, 10–16.
- POPE, S. B. 2000 *Turbulent Flow*. Cambridge: Cambridge University Press.
- RAWAT, S., COSSU, C., HWANG, Y. & RINCON, F. 2015 On the self-sustained nature of large-scale motions in turbulent couette flow. *J. Fluid Mech.* **782**, 515–540.
- SALESKY, S. T., CHAMECKI, M. & BOU-ZEID, E. 2017 On the nature of the transition between roll and cellular organization in the convective boundary layer. *Boundary-Layer Meteorology* **163** (1), 41–68.
- SCAGLIARINI, A., EINARSSON, H., GYLFASSON, A. & TOSCHI, F. 2015 Law of the wall in an unstably stratified turbulent channel flow. *J. Fluid Mech.* **781**, R5.
- SCAGLIARINI, A., GYLFASSON, A. & TOSCHI, F. 2014 Heat-flux scaling in turbulent Rayleigh-Bénard convection with an imposed longitudinal wind. *Phys. Rev. E* **89**, 043012.
- SCHLICHTING, H. & GERSTEN, K. 2000 *Boundary layer theory*, 8th edn. Berlin: Springer Verlag.
- SHEVKAR, P. P., GUNASEGARANE, G. S., MOHANAN, S. K. & PUTHENVEETIL, B. A. 2019 Effect of shear on coherent structures in turbulent convection. *Phys. Rev. Fluids* **4**, 043502.
- SHISHKINA, O., STEVENS, R. J. A. M., GROSSMANN, S. & LOHSE, D. 2010 Boundary layer structure in turbulent thermal convection and its consequences for the required numerical resolution. *New J. Phys.* **12**, 075022.
- SMITS, A. J. & MARUSIC, I. 2013 Wall-bounded turbulence. *Phys. Today* **66** (9), 25–30.
- SMITS, A. J., McKEON, B. J. & MARUSIC, I. 2011 High-Reynolds number wall turbulence. *Annu. Rev. Fluid Mech.* **43**, 353–375.
- SOLOMON, T. H. & GOLLUB, J. P. 1990 Sheared boundary layers in turbulent Rayleigh-Bénard convection. *Phys. Rev. Lett.* **64**, 2382–2385.

- STEVENS, R. J. A. M., BLASS, A., ZHU, X., VERZICCO, R. & LOHSE, D. 2018 Turbulent thermal superstructures in Rayleigh-Bénard convection. *Phys. Rev. Fluids* **3**, 041501(R).
- STEVENS, R. J. A. M., LOHSE, D. & VERZICCO, R. 2011 Prandtl and Rayleigh number dependence of heat transport in high Rayleigh number thermal convection. *J. Fluid Mech.* **688**, 31–43.
- STEVENS, R. J. A. M., VERZICCO, R. & LOHSE, D. 2010 Radial boundary layer structure and Nusselt number in Rayleigh-Bénard convection. *J. Fluid Mech.* **643**, 495–507.
- THURLOW, E. M. & KLEWICKI, J. C. 2000 Experimental study of turbulent Poiseuille-Couette flow. *Phys. Fluids* **12**, 865–875.
- TSUKAHARA, T., KAWAMURA, H. & SHINGAI, K. 2006 DNS of turbulent Couette flow with emphasis on the large-scale structure in the core region. *J. Turb.* **7**, N19.
- TUCKERMAN, L. S. & BARKLEY, D. 2011 Patterns and dynamics in transitional plane couette flow. *Phys. Fluids* **23** (4), 041301.
- VERZICCO, R. & CAMUSSI, R. 1997 Transitional regimes of low-Prandtl thermal convection in a cylindrical cell. *Phys. Fluids* **9**, 1287–1295.
- VERZICCO, R. & CAMUSSI, R. 2003 Numerical experiments on strongly turbulent thermal convection in a slender cylindrical cell. *J. Fluid Mech.* **477**, 19–49.
- VERZICCO, R. & ORLANDI, P. 1996 A finite-difference scheme for three-dimensional incompressible flow in cylindrical coordinates. *J. Comput. Phys.* **123**, 402–413.
- XIA, K.-Q. 2013 Current trends and future directions in turbulent thermal convection. *Theor. Appl. Mech. Lett.* **3**, 052001.
- ZHU, X., MATHAI, V., STEVENS, R. J. A. M., VERZICCO, R. & LOHSE, D. 2018*a* Transition to the ultimate regime in two-dimensional Rayleigh-Bénard convection. *Phys. Rev. Lett.* **120**, 144502.
- ZHU, X., PHILLIPS, E., ARZA, V. S., DONNERS, J., RUETSCH, G., ROMERO, J., OSTILLA-MÓNICO, R., YANG, Y., LOHSE, D., VERZICCO, R., FATICA, M. & STEVENS, R. J. A. M. 2018*b* AFiD-GPU: a versatile Navier-Stokes solver for wall-bounded turbulent flows on GPU clusters. *Comput. Phys. Commun.* **229**, 199–210.